LANGMUIR

pubs.acs.org/Langmuir Article

Spontaneous Multi-scale Supramolecular Assembly Driven by Noncovalent Interactions Coupled with the Continuous Marangoni Effect

Ce Shi and Xinghai Shen*

Cite This: *Langmuir* 2024, 40, 6980−6989 Read Online

ACCESS | Metrics & More | Article Recommendations | Supporting Information

ABSTRACT: Reported herein is the multi-scale supramolecular assembly (MSSA) process along with redox reactions driven by supramolecular interactions coupled with the spontaneous Marangoni effect in ionic liquid (IL)-based extraction systems. The black powder, the single sphere with a black exterior, and the single colorless sphere were formed step by step at the interface when an aqueous solution of $KMnO_4$ was mixed with the IL phase 1-(2-hydroxyethyl)-3-methylimidazolium bis(trifluoromethylsulfonyl) imide ($C_2OHmimNTf_2$) bearing octyl(phenyl)-*N*,*N*-diisobutylcarbamoylmethylphosphine oxide (CMPO). The mechanism of the whole process was studied systematically. The phenomena were related closely to the change in the valence state of Mn. The MnO_4^- ion could be reduced quickly to δ-MnO_2 and further to Mn^{2+} slowly by the hydroxyl-functionalized IL $C_2OHmimNTf_2$. Based on Mn^{2+}, $Mn(CMPO)_3^{2+}$, elementary building blocks (EBBs), and $[EBB]_n$ clusters were generated step by step. The $[EBB]_n$ clusters with the large enough size that were transferred to the interface, together with the remaining δ-MnO_2, assembled into the single sphere with a black exterior, driven by supramolecular interactions coupled with the spontaneous Marangoni effect. When the remaining δ-MnO_2 was used up, the mixed single sphere turned completely colorless. It was found that the reaction site of C_2OHmim^+ with Mn(VII) and Mn(IV) was distributed mainly at the side chain with a hydroxyl group. The MSSA process presents unique spontaneous phase changes. This work paves the way for the practical application of the MSSA-based separation method developed recently. The process also provides a convenient way to observe in situ and characterize directly the continuous Marangoni effect.

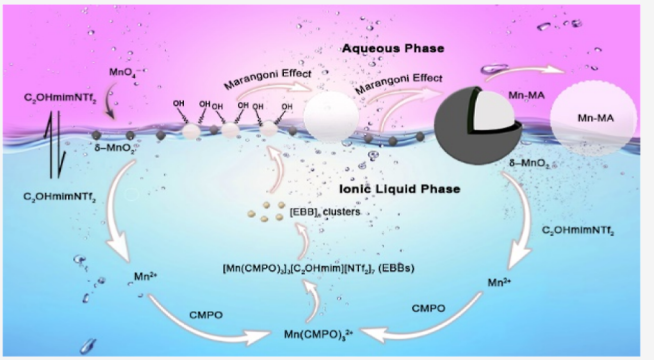

INTRODUCTION

It is well-known that supramolecular chemistry aims at developing complex chemical systems through noncovalent intermolecular forces, and self-organization drives toward the systems of increasing complexity, toward more and more complex forms of matter.[1−6] So far, a large number of supramolecular materials have been developed.[7−13] However, most supramolecular systems investigated at the present time occupy generally the space between the molecular and the nano- to meso-scale worlds.[14] In our previous work, the spontaneous supramolecular process covering molecular, mesoscopic, and macroscopic levels was realized in the ionic liquid (IL)-based extraction system, which was denominated as the multi-scale supramolecular assembly (MSSA).[15−19] When mixing the IL 1-(2-hydroxyethyl)-3-methylimidazolium bis(trifluoromethylsulfonyl) imide ($C_2OHmimNTf_2$) bearing octyl(phenyl)-*N*,*N*-diisobutylcarbamoylmethylphosphine oxide (CMPO) and an aqueous solution of metal ions in the presence of HNO_3, visible spherical assemblies were first formed at the IL−water interface, and then, they further assembled into a single macroscopic assembly (MA) sphere in the glassy state.[15,16] The clear picture of a four-step assembly mechanism of the spontaneous MSSA process was depicted.[16] The structures at four levels, i.e., the complex ions, elementary building blocks (EBBs), $[EBB]_n$ clusters, and the single MA sphere were formed step by step. The selectivity in traditional solvent extraction is generally based on the difference in the pattern or strength of the coordination of metal ions with an extractant at the microscale. Differently, the MSSA-based extraction process could be adjusted simultaneously by factors at micro-, meso-, and macro-scales, and a new concept, i.e., multi-scale selectivity (MSS) was therefore suggested.[16] The effective acid and radiation resistance as well as the high selectivity led us to believe that the MSSA-based extraction strategy has great potential for the separation of metal

Received: January 1, 2024
Revised: March 8, 2024
Accepted: March 10, 2024
Published: March 21, 2024

https://doi.org/10.1021/acs.langmuir.4c00003
Langmuir 2024, 40, 6980−6989

ions in either nonradioactive or radioactive environments, especially in spent nuclear fuel reprocessing.[17]

The Marangoni effect is referred to as the phenomenon that a temperature or concentration gradient causes an interfacial tension gradient, which naturally makes the liquid flow from the low to high surface tension region.[20,21] Specifically, the fourth step of the MSSA process aforesaid is the macroscopic supramolecular assembly at the interface, and the spontaneous and continuous Marangoni effect was inferred to be the driving force.[16] On the contrary, in the traditional solvent extraction systems, the mass transfer and the corresponding solutal Marangoni effect are usually transient processes and thus difficult to be observed directly.[22−24] The effect of the Marangoni convection on the extraction process is a result of the comprehensive consequence of the initial solute concentration, the interface behavior, the surfactant, and so forth. The mass transfer process would be disturbed when the Marangoni convection occurred.[23] The research on the Marangoni effect helps us understand the mechanism of interphase mass transfer. The MSSA process makes a direct observation of the continuous Marangoni effect possible, and thus, the influence on the mass transfer can be elucidated better in extraction systems. The Marangoni effect also plays an important role in many other processes such as design of self-propelled particles[25] and motion of living organisms.[26−28] To investigate the Marangoni effect, physicists introduced surfactants on the air−water interface through a steady point source.[26,29] But low surfactant diffusivity causes concentration measurements at the interface to be difficult during Marangoni flow. Simultaneous access to bulk and surface concentrations, the Marangoni effect and sorption kinetics as well as their subsequent correlation with one another remain great challenges.[26,29] The MSSA process can provide in situ descriptions on the continuous and spontaneous Marangoni flow.[30−32] Insights into the Marangoni effect can also contribute to the understanding of biological phenomena like spreading bacterial colonies[33,34] as well as motion and defense of living organisms.[27]

So far, it has been found that the MA spheres could be formed with UO_2^{2+}, Fe^{3+}, Al^{3+}, Eu^{3+}, Ce^{3+}, Sr^{2+}, Cu^{2+}, Zn^{2+}, Pb^{2+}, and Ln^{3+} as targets.[15,16] Whether the oxometalates such as MnO_4^- and $Cr_2O_7^{2-}$ could be extracted and used as targets participating in the MSSA process remains to be ascertained. In addition, the strong oxidation property of MnO_4^- in the IL phase may give rise to new phenomena in the MSSA system.[35−37] The selective separation between MnO_4^- and $Cr_2O_7^{2-}$ is expected to help us understand the concept of MSS. Hopefully, insights into the MSSA process of the MnO_4^--based system can provide essential information on the mechanism of the Marangoni effect.

EXPERIMENTAL SECTION

Materials. ILs C_2OHmimNTf$_2$ and C_2mimNTf$_2$ (purities >99%) were provided by the Lanzhou Institute of Chemical Physics, Chinese Academy of Sciences. CMPO (purity >98%) was purchased from WuXi AppTec (Shanghai, China). $KMnO_4$ (AR) and $MnSO_4{\cdot}H_2O$ (AR) were purchased from Sinopharm Chemical Reagent Co., Ltd. (Beijing, China). The structures of C_2OHmimNTf$_2$, C_2mimNTf$_2$, and CMPO are shown in Figure S1. Ultra-pure water (18.2 MΩ·cm) was used throughout the experiments.

Instruments. Infrared (IR) spectra were measured at room temperature on a Fourier transform infrared (FT-IR) spectrometer (Nicolet is50, Thermo Fisher). The wavenumber was in the range 400 to 4000 cm^{-1}.

The high-resolution mass spectrometry with electrospray ionization (ESI−HRMS) spectra were recorded on a Fourier transform ion cyclotron resonance mass spectrometer, Solarix XR (Bruker, Germany) with 7 T (Capillary −3 kV, Dry Temp 180 °C, averaged 8 scan). The MA samples were dissolved in dimethyl sulfoxide with a concentration of about 200 μg/mL before ESI−HRMS measurements.

Dynamic light scattering (DLS) measurements of the ethanol solutions were performed on a Malvern Nano ZS90 instrument (Malvern Instruments, UK) at a scattering angle of 90° (wavelength: 633 nm) at 298 K. A He−Ne laser with a power of 4 mW was used as the light source. The Malvern General Purpose method provided by Malvern was utilized to analyze the autocorrelation function and calculate the distribution of the diffusion coefficient (D) of the particles. The parameter D was converted into an effective hydrodynamic radius (R_H) by using the Stokes−Einstein equation. The samples were centrifuged under 4000 rpm for 10 min, and the supernatant was taken for the DLS measurements.

The pH meter (Delta 320, Mettler-Toledo, Switzerland) was adopted to determine the acidity of aqueous solutions.

The X-ray photoelectron spectroscopy (XPS) measurements were performed by using an ESCALAB 250Xi spectrometer (Thermo, USA) at room temperature. Monochromatized Kα radiation was utilized as the X-ray source. The measurements were conducted in the reflection mode geometry.

Magnetic susceptibility measurements were carried out on a Quantum Design SQUID magnetometer MPMS-3, which operated between 3.0 and 300 K for a dc-applied field of 2000 Oe. For anisotropic species microcrystals, the sample was wrapped in a vacuum film in a glovebox in order to avoid oxidation and torquing of the crystallites. The sample mulls were contained in a calibrated gelatin capsule held in the center of a drinking straw that was fixed at the end of the sample rod.

The powder X-ray diffraction (PXRD) pattern was recorded on a Rigaku Dmax-2000 diffractometer (Japan) with Cu Kα radiation.

Gas chromatography (GC)−MS was carried out using a GC mass spectrometer (QP2010/T8050, Shimadzu, Japan) for the identification of oxidation products of the ILs. The aqueous phase was extracted with a mixed solvent of benzene/ethyl acetate/ether (2:2:1). The optimal detection conditions were as follows: Agilent capillary column, HP-5 ms (30 m × 0.25 mm × 0.25 mm); carrier gas, He (1.0 mL/min); temperature program, column oven temperature, 43 °C; heating rate, 10 °C/min; final temperature, 250 °C; injection temperature, 250 °C; injection mode, splitless; injected sample volume, 2 μL; MS detector, ionization mode, EI (70 eV); ion source temperature, 230 °C; interface temperature, 270 °C; and scan mode, full scan.

Inductively coupled plasma−atomic emission spectrometry (ICP−AES, Leeman, USA) with the relative standard deviation below 5% was employed to determine the exact concentrations of metal ions in the aqueous phase. The IL phases and MA phases were digested by a Microwave Digestion System (Mars6 Xpress, CEM, America) before ICP−AES measurements.

Elemental analysis was performed on an elemental analyzer (vario EL, Elementar Analysensysteme GmbH, Germany) with carbon, oxygen, and hydrogen element contents measured. The Mn element content was determined by ICP−AES after digesting the MA sphere with the desired weight.

Confocal images and movies were taken by a laser scanning confocal microscope (Nikon A1R-si, Japan) in the TD mode. The confocal image with the IL−water interface parallel to the beam was obtained as follows: a drop of 60 mM CMPO in C_2OHmimNTf$_2$ was introduced to a 35 mm confocal dish. Then, a drop of 10 mM $MnSO_4$ in 0.1 mM HNO_3 was also introduced to the dish, and it was as close as possible to the IL drop. The confocal dish was rocked slightly, and so, the drops would contact with each other. And then, the system was monitored continuously with the beam parallel to the IL−water interface. The confocal image with the IL−water interface vertical to the beam was obtained as follows: a small drop of 60 mM CMPO in C_2OHmimNTf$_2$ was introduced to a 35 mm confocal dish. Then, a drop of 10 mM $MnSO_4$ in 0.1 mM HNO_3 was also introduced to the dish, and it could cover the IL drop. And then, the system was observed with the beam parallel to the IL−water interface.

Transmission electron microscopy (TEM) was examined on a TEM instrument (FEI Tecnai T20, America).

https://doi.org/10.1021/acs.langmuir.4c00003
Langmuir 2024, 40, 6980−6989

The N_2 adsorption−desorption isotherm was investigated on an Accelerated Surface Area and Porosimetry System (ASAP2010, Micrometer, America). The surface area and pore volume were calculated based on the Barrett−Emmett−Teller (BET) model.

Methods. For the preparation of the MA sample, we took the sample from the CMPO−C_2OHmimNTf$_2$/$KMnO_4$ system as an example. Working solutions of 60 mM CMPO were prepared by dissolving CMPO with the desired weight in C_2OHmimNTf$_2$. $KMnO_4$ solutions for extraction experiments were made up by dissolving weighted $KMnO_4$ in certain concentrations of HNO_3 solutions. Equal volumes of 10 mM $KMnO_4$ in 0.1 M HNO_3 and 60 mM CMPO in C_2OHmimNTf$_2$ were mixed in a vial at 25 °C. The mixture was left to stand and observed for 1 week without stirring. A distinct water−IL interface was formed after standing for 1 min, and then, a large amount of black powder was formed and deposited at the interface. The powder at the interface aggregated into a single sphere with black exterior 48 h later, which gradually turned complete colorless 5 d later. The colorless macroscopic sphere was identified as Mn−MA. The MA sphere was taken out with a tweezer, and the remaining IL and water on the surface were flushed by ethanol. Then, MA was placed in a vacuum drying oven for eliminating ethanol before structural characterizations.

For comparison, the preparation procedure of Mn-MA from the CMPO−C_2OHmimNTf$_2$/$MnSO_4$ system is also listed as follows. $MnSO_4$ solutions were prepared at certain concentrations of HNO_3. Equal volumes of 10 mM $MnSO_4$ in 0.1 M HNO_3 and 60 mM CMPO in C_2OHmimNTf$_2$ were mixed together in a vial at 25 °C. Several colorless spheres appeared at the IL−water interface. The mixture was left for 1 week without stirring, and the assemblies spontaneously converged into one single MA sphere.

RESULTS AND DISCUSSION

As shown in Figure 1a, the MSSA experiments in the CMPO/C_2OHmimNTf$_2$ system with MnO_4^- as the target are carried out, and the process is much different from that with various metal cations reported in our previous work.[15,16] Equal volumes of 10 mM $KMnO_4$ in 0.1 M HNO_3 and 60 mM CMPO in C_2OHmimNTf$_2$ were mixed in a vial at 25 °C. The mixture was left standing for 1 week observation without stirring. A distinct water−IL interface was formed immediately, and then, a large amount of black powder was formed and deposited at the interface. Apparently, the powder at the interface aggregated into a single sphere with black exterior 48 h later, and the sphere gradually turned colorless 5 d later. The vital questions concern the mechanism of the above MSSA process as well as the key role that the Marangoni effect plays.

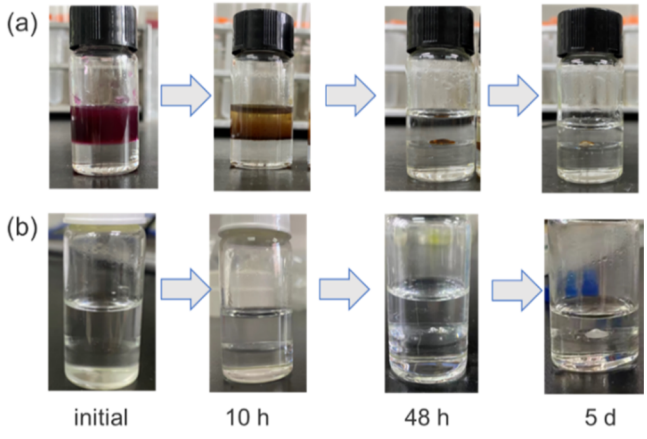

Figure 1. Pictures of the MSSA processes left for 10 h, 48 h, and 5 d at 25 °C after the solution of 60 mM CMPO in C_2OHmimNTf$_2$ was mixed with the aqueous solutions (pH = 1) of 10 mM $KMnO_4$ (a) and 10 mM $MnSO_4$ (b).

For comparison, MSSA experiments in the CMPO−C_2OHmimNTf$_2$ system with Mn^{2+} were also performed. Equal volumes of 10 mM $MnSO_4$ in 0.1 M HNO_3 and 60 mM CMPO in C_2OHmimNTf$_2$ were mixed in a vial at a constant temperature. The mixture was left and observed for 5 d without stirring. As presented in Figure 1b, many macroscale supramolecular assemblies appeared at the interface after the distinct water−IL interface formed, and these macroscopic assemblies spontaneously aggregated into one single colorless MA sphere. The process is similar to that of systems with UO_2^{2+} and other divalent metal ions.[15,16] To make a distinction, the colorless MA spheres from the systems containing $KMnO_4$ and $MnSO_4$ are denoted as Mn-MA-1 and Mn-MA-2, respectively.

Mechanism of the MSSA Process in the CMPO−C_2OHmimNTf$_2$/$KMnO_4$ System. The MSSA system with MnO_4^- presents unique spontaneous phase changes concerning liquid, solid, and glassy states. It is necessary to figure out the structures of all generated species in the interface during the MSSA process.

First, we tried to clarify the specific structure of the final product, Mn-MA-1. From the XPS spectrum (Figure 2a), the peaks of the elements C, N, O, F, P, S, and Mn are all observed, indicating that both CMPO and the anion of C_2OHmimNTf$_2$ participate in the formation of Mn-MA-1. Unfortunately, the signal-to-noise ratio in the XPS spectrum of Mn 2p is too high to recognize the valence state of Mn. The strong magnetism, as shown in Figure 2b, is supposed to lead to the high signal-to-noise ratio, and thus, Mn may be bivalent. The speculation is confirmed by the ESI−HRMS results (Figure 2c,d). The peaks appear at m/z 638.4, 1149.5, and 1556.8 in the positive mode and at 279.9 in the negative mode, which are attributed to $Mn(CMPO)_3^{2+}$, $Mn(CMPO)_2(NTf_2)^+$, $Mn(CMPO)_3(NTf_2)^+$, and NTf_2^-, respectively. To enhance the precision and accuracy, the experimental and theoretical isotopic patterns of the three cations are shown in Figure S2. It can be concluded from the above results that Mn(VII) was reduced to Mn(II) at the end of the MSSA process. The MSSA process with MnO_4^- was coupled with the redox reactions, resulting in a new phenomenon in this work.

The MSSA process for the CMPO−C_2OHmimNTf$_2$/$MnSO_4$ system should be similar to that of the systems containing UO_2^{2+} or other metal cations as reported in our previous work.[15,16] The four-step mechanism of the MSSA process for metal cations has been revealed already.[16] Similarly, the structures at four levels, i.e., the complex ions, EBBs, $[EBB]_n$ clusters, and Mn-MA-2, are supposed to be formed step by step. Provided that the structures of Mn-MA-1 and Mn-MA-2 are the same, there should be similarities between the mechanisms for the above two MSSA systems concerning Mn. The same peaks at m/z 638.4, 1149.5, and 1556.8 in the positive mode and 279.9 in the negative mode can be seen in the ESI−HRMS spectrum of Mn-MA-2 (Figure S3a,b), which is the first evidence confirming that it has the same structure as that of Mn-MA-1. The experimental isotopic patterns of $Mn(CMPO)_3^{2+}$, $Mn(CMPO)_2(NTf_2)^+$, and $Mn(CMPO)_3(NTf_2)^+$ in Mn-MA-2 are shown in Figure S4, in agreement with the experimental patterns of Mn-MA-1 and theoretical patterns. More evidence comes from the exactly same FT-IR results between Mn-MA-1 and Mn-MA-2 (Figure 2e), in which absorptions corresponding to both the cation and anion of C_2OHmimNTf$_2$ are found. For example, the peaks at 1135 and 1186 cm^{-1} are ascribed to the SO_2 symmetric stretch in

https://doi.org/10.1021/acs.langmuir.4c00003
Langmuir 2024, 40, 6980−6989

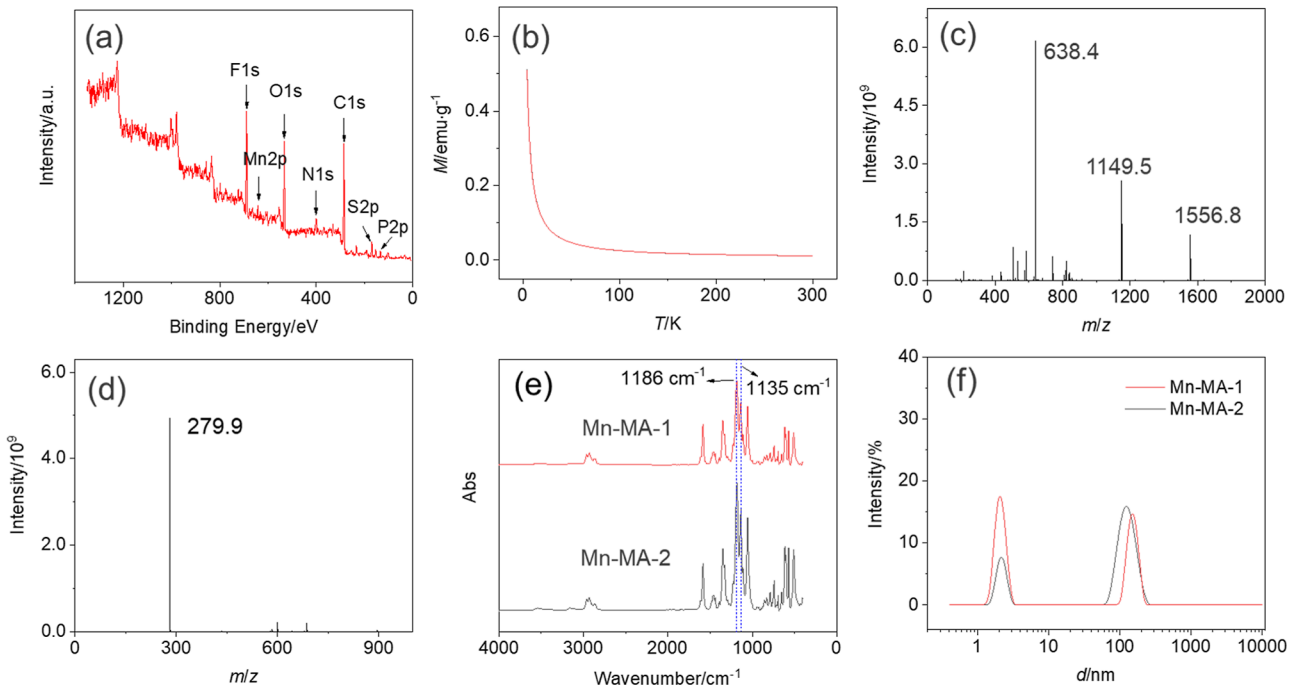

Figure 2. Structural characterizations on Mn-MA-1 and Mn-MA-2. (a) XPS spectrum of Mn-MA-1. (b) $M-T$ curve of Mn-MA-1. ESI−HRMS spectra of Mn-MA-1 in the positive mode (c) and in the negative mode (d). (e) FT-IR spectra of Mn-MA-1 and Mn-MA-2. (f) DLS results of Mn-MA-1 and Mn-MA-2 dissolved in ethanol.

NTf_2^- and the imidazole ring symmetric stretch in C_2OHmim^+, respectively.[38] Therefore, it can be concluded that both Mn-MA-1 and Mn-MA-2 are composed of $Mn(CMPO)_3^{2+}$, C_2OHmim^+, and NTf_2^-. Further, C/H/N element contents were determined by elemental analysis, and the Mn element content was determined by ICP−AES after digesting the MA sphere with the desired weight. As shown in Table S1, the chemical compositions of Mn-MA-1 and Mn-MA-2 are the same, in close accordance with that of $Mn(CMPO)_3^{2+}$:C_2OHmim^+:NTf_2^- = 3:1:7 in a molar ratio.

The size distributions were measured by DLS after dissolving Mn-MA-1 and Mn-MA-2 in ethanol (Figure 2f). According to the four-step mechanism,[16] the peaks at about 2.1 and 130 nm in the DLS result of Mn-MA-2 are ascribed to the sizes of EBB and $[EBB]_n$ clusters, respectively. The $[Mn(CMPO)_3]_3[C_2OHmim][NTf_2]_7$ unit acts as an EBB in the MSSA process, which is inferred from the EBB structure with UO_2^{2+} and other cations reported in our previous work.[16] The peaks at about 2.1 and 130 nm are also observed in the DLS result of Mn-MA-1, indicating that EBB and $[EBB]_n$ clusters are formed as well in the system with MnO_4^-. The complex ion $[Mn(CMPO)_3]^{2+}$ interacts with the cation and anion of the IL, leading to the formation of EBBs. The EBBs can further aggregate into $[EBB]_n$ clusters with a larger size, as demonstrated by the peak at 130 nm in Figure 2f. The structure of $[EBB]_n$ clusters with UO_2^{2+} and other cations was investigated by force field simulations, and it was found that the partial numerical density along the three directions of the space was nonuniform and the radial distribution function $g(r)$ trended to 1 with little fluctuations, revealing the nature of the MA sphere as a glassy state matter.[16]

To sum up, all the characterizations confirmed the same structures of Mn-MA-1 and Mn-MA-2, although the initial valences of Mn are different. Next, characterizations on the black intermediates are necessary. The first challenge is the separation between the black powders and the sphere with a black exterior before characterizations.

As mentioned above, the redox reactions between MnO_4^- and $C_2OHmimNTf_2$ occurred in the MSSA process, and Mn(II) was formed ultimately. To simplify the complex system, we tried to remove the extractant CMPO and figure out the redox reactions in the $C_2OHmimNTf_2/KMnO_4$ system. The pictures of the system with the reactions going are shown in Figure 3a, and the phenomenon is totally different from that of the system containing CMPO. At first, it can also be seen that the black powders are formed in the aqueous phase and deposited at the

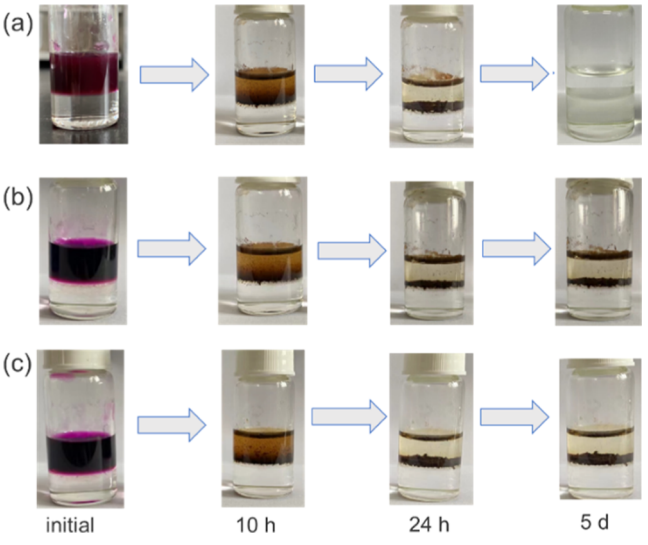

Figure 3. Pictures of the systems left for 10 h, 24 h, and 5 d at 25 °C after the aqueous solution of 10 mM $KMnO_4$ (pH = 1) was mixed with $C_2OHmimNTf_2$ itself (a), $C_2mimNTf_2$ itself (b), and the solution of 60 mM CMPO in $C_2mimNTf_2$ (c).

https://doi.org/10.1021/acs.langmuir.4c00003
Langmuir 2024, 40, 6980−6989

water−IL interface. However, the powdery intermediates could not assemble into a single black sphere any more. Instead, the powdery intermediates totally disappear, and the system settles into the two transparent phases at equilibrium. Without the formation of the sphere with a black exterior at the interface, we can collect pure powdery intermediates easily, and the sample is washed by ethanol several times and placed in a vacuum drying oven for eliminating ethanol before characterizations.

Different from that of Mn-MA-1, the spectra of the elements C, N, O, and Mn are observed in the XPS spectrum of the black powder (Figure 4a). It can be seen from Figure 4b that the Mn 2p spectrum exhibits two peaks at 642.4 and 654.0 eV, which can be referred to as the binding energies of $2p_{3/2}$ and $2p_{1/2}$, respectively. The energy separation between the two peaks is 11.6 eV, which is in agreement with the XPS results of manganese oxide in the literature.[39,40] As discussed in detail by Nesbitt,[41,42] the Mn $2p_{3/2}$ spectrum reveals Mn(IV) and Mn(III) in the near-surface region (uppermost 30 Å) of the coating. The spectral fits to the Mn $2p_{3/2}$ spectrum are shown in Figure 4b, and the peak parameters used to fit the spectra are referred from the literature.[41−43] It can be concluded that Mn(IV) is the main state of manganese in the powder, while Mn(III) is the minor. It is suggested that the powder may be birnessite (δ-MnO_2) because the oxidation state of manganese in δ-MnO_2 is mainly Mn(IV) with little Mn(III) and the average states commonly fall between 3.6 and 3.8.[44] Further evidence is obtained from the PXRD pattern (Figure 4c), which exhibits diffraction peaks at about 11.9, 36.8, and 66.0°, corresponding to the (001), (111), and (020) planes, respectively.[44] The rather low diffractions peaks are ascribed to the low crystallinity according to the morphological characterizations shown in Figure S5, which is in agreement with the literature.[45,46] The presence of porous nanostructures in the TEM pattern can contribute to a broad background in the XRD pattern. Therefore, it is believed that the first step of the MSSA process is the redox reactions between MnO_4^- and $C_2OHmimNTf_2$ forming the powdery δ-MnO_2, and a small number of imidazolium cations are attached on δ-MnO_2 according to Figure 4a. Then, δ-MnO_2 was deposited at the water−IL interface.

In the N_2 adsorption−desorption isotherm of δ-MnO_2 (Figure S6), there appears an obvious hysteresis loop associated with the filling of the mesopores, which is in agreement with the TEM images (Figure S5). The calculated BET surface area and pore volume of δ-MnO_2 are 137.1 m^2/g and 0. 161 cm^3/g, respectively. The above results indicate the strong oxidizing property of the generated δ-MnO_2 during the MSSA process. Therefore, the disappearance of δ-MnO_2 from the interface of the system without CMPO (Figure 3a) is due to the reduction of δ-MnO_2 to Mn^{2+} by the IL $C_2OHmimNTf_2$. To further verify the idea, CMPO was introduced to the system again after the system without CMPO reached an equilibrium. As shown in Figure S7a,b, the colorless Mn−MA can be formed spontaneously again when CMPO is introduced to the mixture of the aqueous solution of 10 mM $KMnO_4$ (pH = 1) and $C_2OHmimNTf_2$. The process was exactly the same as that of the CMPO−$C_2OHmimNTf_2$/$MnSO_4$ system shown in Figure 1b, indicating that δ-MnO_2 is reduced to Mn^{2+} when the $C_2OHmimNTf_2$/$KMnO_4$ system reaches an equilibrium.

Marangoni Effect in the MSSA Process. From the above results, it is clear that the black powder is δ-MnO_2, which can be further reduced to Mn(II). Nevertheless, it is still a puzzle that the black solid powder can automatically "glue" together into a single sphere with a black appearance in the presence of CMPO, as shown in Figure 1a. The pictures shown in Figure 3a confirm that the powder itself cannot assemble with each other. Therefore, it is assumed that the generated Mn(II) resulted in the formation of the sphere with the black appearance. When the system of 10 mM $KMnO_4$ (pH = 1) mixed with the IL $C_2OHmimNTf_2$ was left for 10 h, a large amount of black

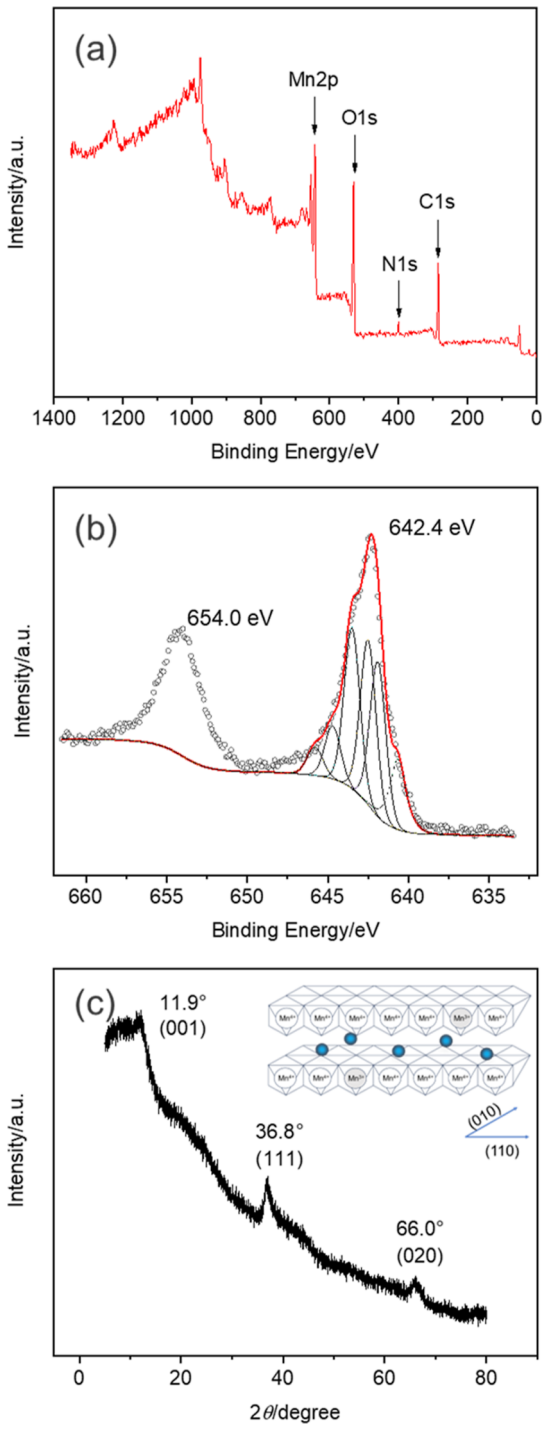

Figure 4. Characterizations of the black powder. (a) XPS broad scan for the surface. (b) XPS spectrum of the Mn 2p region. The open circles represent the XPS data, and the red solid curve is the fit to the data. The black solid curves represent Mn(IV) multiplet peaks, and the dotted curve represents Mn(III) peaks. (c) PXRD pattern (inset: typical structure of δ-MnO_2).

https://doi.org/10.1021/acs.langmuir.4c00003
Langmuir 2024, 40, 6980−6989

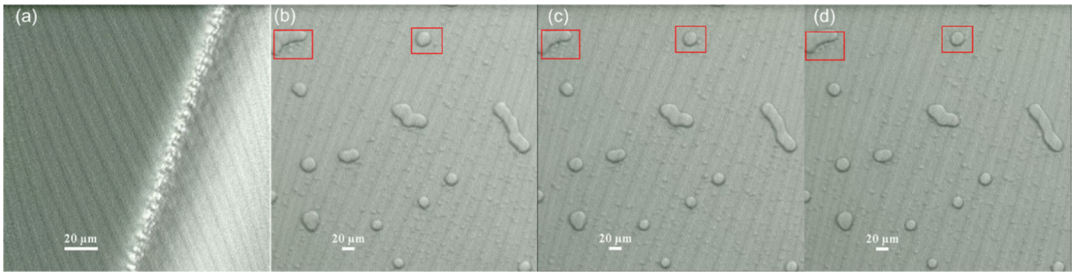

Figure 5. Representative confocal images of the MSSA process. (a) The IL−water interface was parallel to the beam. (b,d) The IL−water interface was vertical to the beam. The interval of the three images is 100 s.

powder was formed, into which the extractant CMPO was introduced, and the corresponding phenomenon is illustrated in Figure S7b. It can be seen that the black sphere is also formed, which turns colorless finally. The result confirmed that CMPO resulted in the formation of a sphere with a black appearance.

We can see from the MSSA process of the system with Mn^{2+} that four level structures, i.e., $Mn(CMPO)_3^{2+}$, EBBs, $[EBB]_n$ clusters, and the single MA sphere, could be formed step by step. It is inferred that a similar process could also occur when MnO_4^- was reduced to Mn^{2+} in the system containing MnO_4^-. The $Mn(CMPO)_3^{2+}$, EBBs, and $[EBB]_n$ clusters can be formed step by step, which is in agreement with the characterization of Mn-MA-1. When the $[EBB]_n$ clusters grow to be large enough in the IL phase, they can stay in the IL phase no longer. Similar to the MSSA process in the UO_2^{2+}-based system,[16] the large-sized $[EBB]_n$ clusters would approach the IL−water interface. Dominguez et al.[47] show theoretically that the active spherical clusters with a significant effect on the properties of the interface, although immobile in bulk, experience a very strong, long-ranged effective force field due to the Marangoni stresses self-induced at the interface. It may give rise to a drift of the particle toward the fluid interface. The spontaneous MSSA process proved the theoretical results experimentally. When the $[EBB]_n$ clusters grow to be large enough in the IL phase, they would transfer to the IL−water interface, which is observed by laser scanning confocal microscopy (Figure 5a). When the IL−water interface is parallel to the beam, we can see the clusters concentrating at the interface instead of remaining in the bulk phase (Supporting Information Movie S1).

The continuous transferring of $[EBB]_n$ clusters from the IL phase to the interface causes a great disturbance on the local distribution of the surface-active IL at the interface. To characterize the Marangoni flow, most studies choose to introduce the droplets of surfactant solutions on thin films. Irzi et al.[25] reported the spontaneous motion of pure water droplets in an oil−surfactant medium. Water from the droplet is solubilized by the reverse micellar solution, creating a concentration gradient of swollen reverse micelles around each droplet. But the transient nature of the induced flow and the small size of the film prevented the validation of the proposed descriptions. In the MSSA system, the distribution of the surface-active IL was disturbed around the $[EBB]_n$ clusters, and thus, the concentration gradient of the ILs was formed. In such a case, both the concentration gradient and interfacial tension gradient are durative, and thus, the spontaneous and continuous Marangoni effect can accompany the whole MSSA process. The $[EBB]_n$ clusters were formed spontaneously without additional disturbance. Therefore, in situ characterizations on the Marangoni effect can be realized by the observations on the MSSA process, as shown in Figure 5b−d. When the IL−water interface is vertical to the beam, it can be seen that the clusters at the interface would move and collide, driven by the spontaneous Marangoni effect, and they would further assemble with each other due to supramolecular interactions (Supporting Information Movie S2).

Generally, tracers are introduced to observe the Marangoni flow. In the MSSA system, the assembly process at the interface of the macroscopic assemblies and δ-MnO_2 driven by the Marangoni effect can be clearly seen from Figure 3c. δ-MnO_2 was driven to a single sphere as tracers. The redox reactions between $C_2OHmimNTf_2$ and δ-MnO_2 occurred continuously, and the corresponding product Mn^{2+} was generated. Mn^{2+} could assemble into colorless MA, and thus, the sphere turns colorless from black. It can be concluded from the above results that it is the Marangoni effect during the MSSA process that drives powdery δ-MnO_2 to assemble into one single black sphere. The black δ-MnO_2 powder acts as the tracer agent to display the Marangoni effect-driven movement viably.

In summary, the mechanism of the MSSA process in the CMPO−$C_2OHmimNTf_2$/$KMnO_4$ system is revealed, as shown in Figure 6. First, Mn(VII) is reduced to powdery δ-MnO_2 by

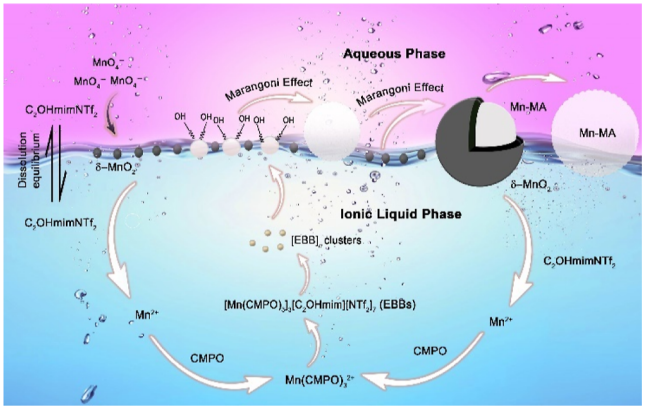

Figure 6. Mechanism of the MSSA process in the CMPO−$C_2OHmimNTf_2$/$KMnO_4$ system.

the IL $C_2OHmimNTf_2$, and the solid phase is formed at the interface. Second, δ-MnO_2 is reduced to Mn^{2+} slowly, and meanwhile, complex ion $Mn(CMPO)_3^{2+}$, EBBs, and $[EBB]_n$ clusters are formed based on the generated Mn^{2+} step by step. Third, when the $[EBB]_n$ clusters grow to be large enough, they can stay in the IL phase no longer and would transfer to the IL−water interface. The glassy matter phase is formed, and it results in the continuous and spontaneous Marangoni effect. The remaining δ-MnO_2 and large $[EBB]_n$ clusters at the interface are driven to approach each other and assemble into a single sphere

https://doi.org/10.1021/acs.langmuir.4c00003
Langmuir 2024, 40, 6980−6989

due to supramolecular interactions. Fourth, the continuous redox reaction happens between the remaining δ-MnO_2 in the single black sphere and the IL Mn^{2+}, which rationalizes the phenomenon that the black sphere turns colorless. The solid phase disappears in the end, and the system presents three phases, i.e., aqueous phase, IL phase, and glassy matter phase. Supramolecular interactions coupled with the spontaneous and continuous Marangoni effect drive the whole MSSA process. Insights into the process can provide an easy way to realize in situ characterizations on the continuous Marangoni effect in the extraction system.

MSS-Based Separation. In the traditional liquid−liquid system, the selectivity is generally due to the difference in the coordination chemistry at the microscale.[48−50] The oxidation state control of metal ions is an effective and widely used method to change the strength of the coordinating effect between metal ions and extractants. Classically, the separation of U(VI) and Pu(IV) is realized by reducing Pu(IV) to Pu(III) in spent nuclear fuel reprocessing. Recently, Xu's group reported the ultra-efficient Am/Ln and Am/Cm separation method based on oxidation state control.[51,52]

The concept MSS was suggested based on the MSSA extraction method in our previous work.[16] The remarkable discrimination can originate from multiple effects, including supramolecular recognition from microscopic to macroscopic scales and the kinetic control at the interface.[16,53] Theoretical calculations confirmed that the extraction efficiency and selectivity are significantly affected by the capacity of EBBs solved in the IL phase assembling to $[EBB]_n$ clusters.[16] Herein, we believe that the idea of oxidation state control can further enhance the selectivity of the MSSA extraction method in the redox reactions involved in the MSSA process.

The MSSA experiments for the $K_2Cr_2O_7$ system were also carried out. Cr-MA was formed eventually without powdery intermediate products. The peaks of the elements C, N, O, F, P, S, and Cr are all observed from the XPS broad scan spectrum of Cr-MA (Figure S8a), indicating that both CMPO and the anion of $C_2OHmimNTf_2$ participate in the formation of Cr-MA, which is similar to that of Mn-MA-1. The spectral fit to the Cr 2p spectrum is shown in Figure S8b, and the peak parameters used to fit the spectra are referred from the literature.[43] The spectral fit is in agreement with that of $Cr(OH)_3$,[43] suggesting that Cr(VI) was directly reduced to Cr(III), which could participate in the formation of Cr-MA. The different processes of Mn-MSSA and Cr-MSSA could give a new pathway to realize MSS in the separation between Mn(VII) and Cr(VI). In addition, both the FT-IR spectroscopy and DLS results (Figure S9) indicate that the structure of Cr-MA is similar to that of Mn-MA. Absorptions of both the cation and anion in $C_2OHmimNTf_2$ are found in the FT-IR spectra (Figure S9a). The peaks at 1135 and 1186 cm^{-1} are ascribed to the symmetric stretch of SO_2 in NTf_2^- and that of the imidazole ring in C_2OHmim^+, respectively.[38] The DLS result (Figure S9b) of Cr-MA dissolved in ethanol confirms the existence of EBBs in the formation of Cr-MA. The peak at about 2.0 nm can be ascribed to the size of the EBB.

When the solution of 60 mM CMPO in $C_2OHmimNTf_2$ was mixed with the aqueous solution of 10 mM $KMnO_4$ and 5 mM $K_2Cr_2O_7$ at 25 °C, a large amount of black powder was formed immediately. The system was left for 1 h, and the distributions of metal ions in the IL phase, aqueous phase, and the δ-MnO_2/Mn-MA phase were determined. As shown in Figure 7, over 99% of Mn is transferred to the δ-MnO_2/Mn-MA phase at the interface. By contrast, 98% of the Cr remains in the aqueous phase. This

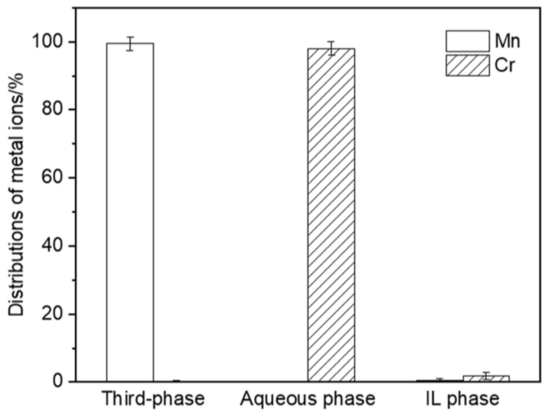

Figure 7. Percentage of metal ions in the three phases (aqueous phase, IL phase, and δ-MnO_2/Mn-MA phase) at equilibrium at 10 °C.

phenomenon is due to the fact that the rate of the redox reaction between Mn(VII) and the IL is much higher than that of Cr(VI). Mn(IV) and Mn(II) can be transferred to the δ-MnO_2/Mn-MA phase at the interface. By this new approach, the separation with high selectivity between Mn(VII) and Cr(VI) is realized, which is a successful example of oxidation state control involved with MSS.

In the traditional liquid−liquid extraction system, oxidation state control of metal ions aims at changing the strength of the coordinating effect between metal ions and the extractant at the microscale, leading to selective extraction. Differently, in the MSSA-based extraction system, both Mn-MA and Cr-MA can be formed after oxidation state control, indicating that there is no significant difference between the coordinating effect of Mn(II) with CMPO and that of Cr(III) at the microscale. The outstanding selectivity is attributed to not only the competitive coordinating effect at the microscale but also supramolecular recognition from mesoscopic to macroscopic scales and the kinetic control at the interface.

To figure out the mechanism of the different MSSA processes, it is necessary to explore the oxidation mechanism of the IL $C_2OHmimNTf_2$ in the above MSSA process. So far, the research has been focused on the oxidation mechanism of alkyl imidazolium-type ILs.[54−57] Qu's group reported the oxidation mechanisms of alkene-functionalized imidazolium-type ILs by Fe(VI). It was proved that the reactivities of this kind of ILs toward Fe(VI) mainly depend on the double bonds in the side chain.[58] Therefore, we tried to figure out the effect of the hydroxyl group in the side chain of $C_2OHmimNTf_2$ in the oxidation mechanism.

For comparison with the $C_2OHmimNTf_2/KMnO_4$ system, experiments on the $C_2mimNTf_2/KMnO_4$ systems with and without the extractant CMPO, respectively, were accomplished. The pictures of the systems in different stages are shown in Figure 3b,c. One can see that both of the systems reach equilibrium with the black powder standing at the interface, indicating that $C_2mimNTf_2$ could be oxidized by Mn(VII) but not by δ-MnO_2. It is reported that the primary product in the degradation of $C_2mimNTf_2$ is 1-ethyl-3-methyl-2,4,5-imidazolidinetrione.[55,57] The product was detected in the reacted IL phase from the $C_2mimNTf_2/KMnO_4$ system by GC−MS (Figure S10). 1-Eethyl-3-methyl-2,4,5-imidazolidinetrione cannot further react with Mn(VII) because the volume of the IL phase is equal to that of the aqueous phase and $C_2mimNTf_2$ is significantly in excess for the redox reaction.

https://doi.org/10.1021/acs.langmuir.4c00003
Langmuir 2024, 40, 6980−6989

As mentioned above, C_2OHmimNTf$_2$ can be oxidized by δ-MnO_2 but C_2mimNTf$_2$ cannot. The difference demonstrates that the hydroxyl in the side chain of C_2OHmimNTf$_2$ can significantly lower its chemical stability, and thus, the most reactive site must be the side chain with the hydroxyl group. The evidence comes from the ESI−HRMS results of the reacted IL phase from the C_2OHmimNTf$_2$/$KMnO_4$ system (Figure 8a)

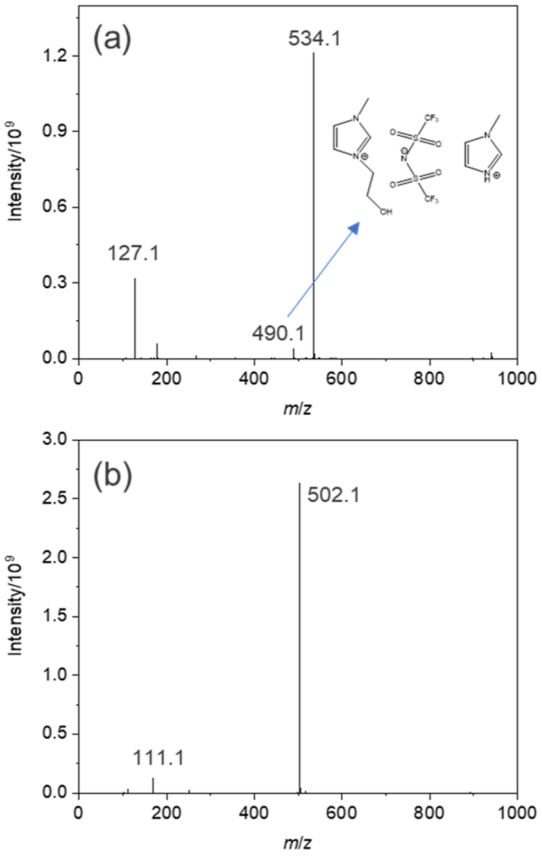

Figure 8. ESI−HRMS spectra of the reacted IL phases from the C_2OHmimNTf$_2$/$KMnO_4$ system (a) and C_2mimNTf$_2$/$KMnO_4$ system (b).

with the peaks at m/z 127.1, 490.1, and 534.1 in the positive mode. The peaks at m/z 127.1 and 534.1, ascribed to C_2OHmim$^+$ and [C_2OHmim·C_2OHmimNTf$_2$]$^+$, respectively, are the characteristic peaks of the IL C_2OHmimNTf$_2$. The peak at m/z at 490.1 nm is assigned to [mim·C_2OHmimNTf$_2$]$^+$, demonstrating the loss of the hydroxyethyl side chain. Similar characterizations were also carried out for the reacted IL phase from the C_2mimNTf$_2$/$KMnO_4$ system, as shown in Figure 8b. The peaks at 111.1 and 502.1 are observed, ascribed to characteristic peaks in the positive range of C_2mimNTf$_2$, C_2mim$^+$, and [C_2mim·C_2mimNTf$_2$]$^+$, respectively. The absence of the third peak confirms the difference in oxidation mechanisms of C_2OHmimNTf$_2$ from that of C_2mimNTf$_2$.

CONCLUSIONS

In this work, the new phenomenon of the MSSA process in an IL-based extraction system with MnO_4^- as the target was reported for the first time, and the mechanism of the whole process was systematically studied. The phenomena are due to the change in the valence state of manganese. Mn(VII) can be reduced quickly by C_2OHmimNTf$_2$ to δ-MnO_2, and it can be further reduced to Mn^{2+} slowly by the IL. Meanwhile, $Mn(CMPO)_3^{2+}$, EBBs, and $[EBB]_n$ clusters are formed step by step. The $[EBB]_n$ clusters transferred to the interface, together with the remaining δ-MnO_2, can assemble into one single black sphere driven by supramolecular interactions coupled with the spontaneous Marangoni effect. Finally, the remaining δ-MnO_2 is used up, and the black sphere turns into colorless Mn-MA-1. And the selective separation of Mn(VII) and Cr(VI) is realized based on oxidation-involved MSS.

The MSSA processes reported herein present unique spontaneous multiphase changes accompanied by spontaneous color changes. The processes provide convenient ways to observe in situ and characterize directly the continuous Marangoni effect, which will contribute to the deep understanding on this essential effect concerned in various areas. This work will pave the way for the practical application of the MSSA-based method on the separation of various metal ions. And it is of great importance in view of the coupling of the Marangoni effect to supramolecular interactions, which gives rise to the successful spanning over an elusive gap between the mesoscopic and macroscopic supramolecular assembly.

ASSOCIATED CONTENT

Supporting Information

The Supporting Information is available free of charge at https://pubs.acs.org/doi/10.1021/acs.langmuir.4c00003.

structures of the ILs and extractant involved in this work; ESI−MS spectra of Mn-MA-2; experimental and theoretical isotopic patterns; C/H/N/Mn contents of relative percentages of Mn-MA-1 and Mn-MA-2; TEM images of δ-MnO_2; N_2 adsorption−desorption isotherms of δ-MnO_2; pictures of $KMnO_4$/C_2OHmimNTf$_2$ systems with the introduction of CMPO; structural characterizations of Cr-MA; generated species from different systems; and mass spectrum identified for the oxidated product 1-ethyl-3-methyl-2,4,5-imidazolidinetrione of C_2mimNTf$_2$ by GC−MS (PDF)

Confocal movie at 5× speed of the CMPO−C_2OHmimNTf$_2$/$MnSO_4$ system with the IL−water interface parallel to the beam (MP4)

Confocal movie at 20× speed of the CMPO−C_2OHmimNTf$_2$/$MnSO_4$ system with the IL−water interface vertical to the beam (MP4)

AUTHOR INFORMATION

Corresponding Author

Xinghai Shen − *Fundamental Science on Radiochemistry and Radiation Chemistry Laboratory, Beijing National Laboratory for Molecular Sciences (BNLMS), Center for Applied Physics and Technology, College of Chemistry and Molecular Engineering, Peking University, Beijing 100871, P. R. China;* orcid.org/0000-0001-8478-7186; Email: xshen@pku.edu.cn

Author

Ce Shi − *Fundamental Science on Radiochemistry and Radiation Chemistry Laboratory, Beijing National Laboratory for Molecular Sciences (BNLMS), Center for Applied Physics and Technology, College of Chemistry and Molecular Engineering, Peking University, Beijing 100871, P. R. China;* orcid.org/0000-0002-2491-5614

Complete contact information is available at:

https://pubs.acs.org/10.1021/acs.langmuir.4c00003

Author Contributions

The manuscript was written through contributions of all authors.

Notes

The authors declare no competing financial interest.

■ ACKNOWLEDGMENTS

This work was financially supported by the National Natural Science Foundation of China (grant no. U1830202) and the Science Challenge Project (TZ2016004). Sincere thanks are given to Jianyuan Qi for the assistance in experiments. We thank Jingyuan Wang, Xiaoran He, and Dr. Wei Pan for their help with XPS, ESI−HRMS, and FT-IR spectroscopy measurements, respectively. The authors acknowledge the Electron Microscopy Laboratory of Peking University, China for the use of the FEI Tecnai T20 TEM system.

■ REFERENCES

(1) Lehn, J. M. *Supramolecular Chemistry. Concepts and Perspectives*; VCH: New York, 1995.
(2) Lehn, J. M. Toward self-organization and complex matter. *Science* **2002**, *295* (5564), 2400−2403.
(3) Lehn, J. M. Toward complex matter: Supramolecular chemistry and self-organization. *Proc. Natl. Acad. Sci. U.S.A.* **2002**, *99* (8), 4763−4768.
(4) Lehn, J. M. From supramolecular chemistry towards constitutional dynamic chemistry and adaptive chemistry. *Chem. Soc. Rev.* **2007**, *36* (2), 151−160.
(5) Lehn, J. M. Perspectives in chemistry-steps towards complex matter. *Angew. Chem., Int. Ed.* **2013**, *52* (10), 2836−2850.
(6) Lehn, J. M. Beyond chemical synthesis: Self-organization?! *Isr. J. Chem.* **2018**, *58* (1−2), 136−141.
(7) Sun, Q.-F.; Iwasa, J.; Ogawa, D.; Ishido, Y.; Sato, S.; Ozeki, T.; Sei, Y.; Yamaguchi, K.; Fujita, M. Self-assembled M24L48 polyhedra and their sharp structural switch upon subtle ligand variation. *Science* **2010**, *328* (5982), 1144−1147.
(8) Wu, Q.; Rauscher, P. M.; Lang, X.; Wojtecki, R. J.; De Pablo, J. J.; Hore, M. J.; Rowan, S. J. Poly[n]catenanes: Synthesis of molecular interlocked chains. *Science* **2017**, *358* (6369), 1434−1439.
(9) Cheng, L.; Liang, C.; Liu, W.; Wang, Y.; Chen, B.; Zhang, H.; Wang, Y.; Chai, Z.; Wang, S. Three-dimensional polycatenation of a uranium-based metal−organic cage: Structural complexity and radiation detection. *J. Am. Chem. Soc.* **2020**, *142* (38), 16218−16222.
(10) Yu, H.-M.; Du, M.-H.; Shu, J.; Deng, Y.-H.; Xu, Z.-M.; Huang, Z.-W.; Zhang, Z.; Chen, B.; Braunstein, P.; Lang, J.-P. Self-assembly of cluster-mediated 3D catenanes with size-specific recognition behavior. *J. Am. Chem. Soc.* **2023**, *145* (46), 25103−25108.
(11) Torresi, S.; Famulari, A.; Martí-Rujas, J. Kinetically controlled fast crystallization of M12L8 poly-[n]-catenanes using the 2,4,6-tris(4-pyridyl)benzene ligand and $ZnCl_2$ in an aromatic environment. *J. Am. Chem. Soc.* **2020**, *142* (20), 9537−9543.
(12) Aoyama, S.; Catti, L.; Yoshizawa, M. Facile processing of unsubstituted π-conjugated aromatic polymers through water-solubilization using aromatic micelles. *Angew. Chem., Int. Ed.* **2023**, *62*, No. e202306399.
(13) Martí-Rujas, J. Connecting metal-organic cages (MOCs) for CO_2 remediation. *Mater. Adv.* **2023**, *4* (19), 4333−4343.
(14) Bohne, C. Supramolecular dynamics. *Chem. Soc. Rev.* **2014**, *43* (12), 4037−4050.
(15) Chen, B. H.; Wu, K. G.; Yang, Y. Q.; Wang, N.; Liu, Y.; Hu, S. L.; Wang, J.; Wen, J.; Hu, S.; Chen, Q. D.; Shen, X. H.; Peng, S. M. A uranium capture strategy based on self-assembly in a hydroxyl-functionalized ionic liquid extraction system. *Chem. Commun.* **2019**, *55* (48), 6894−6897.
(16) Chen, B. H.; Shi, C.; Xiong, S. J.; Wu, K. G.; Yang, Y. Q.; Mu, W. J.; Li, X. L.; Yang, Y. C.; Shen, X. H.; Peng, S. M. Insights into the spontaneous multi-scale supramolecular assembly in an ionic liquid-based extraction system. *Phys. Chem. Chem. Phys.* **2022**, *24* (42), 25950−25961.
(17) Shi, C.; Xiong, S. J.; Li, S. X.; Shen, X. H. Improvement on the radiation stability of multi-scale supramolecular assembly in ionic liquid-based extraction. *J. Phys. Chem. B* **2023**, *127* (33), 7334−7341.
(18) Shi, C.; Shen, X. H. Microscopic, mesoscopic and macroscopic supramolecular assembly in extraction. Specific functions of ionic liquids. *J. Nucl. Radiochem.* **2022**, *44* (1), 1−14.
(19) Shi, C.; Xiong, S. J.; Shen, X. H. Strontium extraction based on macroscopic supramolecular assembly in ionic liquid system. *J. Nucl. Radiochem.* **2022**, *44* (1), 52−60.
(20) Karbalaei, A.; Kumar, R.; Cho, H. J. Thermocapillarity in microfluidics-a review. *Micromachines* **2016**, *7* (1), 13.
(21) Sun, P.; Huang, K.; Liu, H. In situ study of the competitive adsorption of ions at an organic-aqueous two-phase interface: the essential role of the Hofmeister effect. *Soft Matter* **2019**, *15* (21), 4346−4350.
(22) Jain, A.; Verma, K. K. Recent advances in applications of single-drop microextraction: A review. *Anal. Chim. Acta* **2011**, *706* (1), 37−65.
(23) Chen, J.; Yang, C.; Mao, Z.-S. The interphase mass transfer in liquid−liquid systems with Marangoni effect. *Eur. Phys. J.: Spec. Top.* **2015**, *224* (2), 389−399.
(24) Wang, Z.; Chen, J.; Feng, X.; Mao, Z.-S.; Yang, C. Visual dynamical measurement of the solute-induced Marangoni effect of a growing drop with a PLIF method. *Chem. Eng. Sci.* **2021**, *233*, 116401.
(25) Izri, Z.; van der Linden, M. N.; Michelin, S.; Dauchot, O. Self-propulsion of pure water droplets by spontaneous marangoni-stress-driven motion. *Phys. Rev. Lett.* **2014**, *113* (24), 248302.
(26) Roché, M.; Li, Z.; Griffiths, I. M.; Le Roux, S.; Cantat, I.; Saint-Jalmes, A.; Stone, H. A. Marangoni flow of soluble amphiphiles. *Phys. Rev. Lett.* **2014**, *112* (20), 208302.
(27) Bush, J. W. M.; Hu, D. L. Walking on water: Biolocomotion at the Interface. *Annu. Rev. Fluid. Mech.* **2006**, *38* (1), 339−369.
(28) Herzig, M. A.; Barnes, G. T.; Gentle, I. R. Improved spreading rates for monolayers applied as emulsions to reduce water evaporation. *J. Colloid Interface Sci.* **2011**, *357* (1), 239−242.
(29) Bandi, M. M.; Akella, V. S.; Singh, D. K.; Singh, R. S.; Mandre, S. Hydrodynamic signatures of stationary Marangoni-driven surfactant transport. *Phys. Rev. Lett.* **2017**, *119* (26), 264501.
(30) Li, Y.; Diddens, C.; Prosperetti, A.; Lohse, D. Marangoni instability of a drop in a stably stratified liquid. *Phys. Rev. Lett.* **2021**, *126* (12), 124502.
(31) Dietrich, K.; Jaensson, N.; Buttinoni, I.; Volpe, G.; Isa, L. Microscale marangoni surfers. *Phys. Rev. Lett.* **2020**, *125* (9), 098001.
(32) Trittel, T.; Harth, K.; Klopp, C.; Stannarius, R. Marangoni flow in freely suspended liquid films. *Phys. Rev. Lett.* **2019**, *122* (23), 234501.
(33) Trinschek, S.; John, K.; Thiele, U. Modelling of surfactant-driven front instabilities in spreading bacterial colonies. *Soft Matter* **2018**, *14* (22), 4464−4476.
(34) Harshey, R. M. Bacterial motility on a surface: Many ways to a common goal. *Annu. Rev. Microbiol.* **2003**, *57* (1), 249−273.
(35) Kumar, A.; Jain, N.; Chauhan, S. M. S. Oxidation of benzylic alcohols to carbonyl compounds with potassium permanganate in ionic liquids. *Synth. Commun.* **2004**, *34* (15), 2835−2842.
(36) Safaei-Ghomi, J.; Hajipour, A. R. Mild oxidative deprotection of aromatic hydrazones and semicarbazones with $KMnO_4$ in ionic liquid medium. *Org. Prep. Proced. Int.* **2011**, *43* (4), 372−376.
(37) Lu, Y.-J.; Wong, W.-L.; Chow, C.-F. A surfactant-like ionic liquid with permanganate dissolved as a highly selective epoxidation system. *Catal. Commun.* **2015**, *69*, 25−28.
(38) Noack, K.; Schulz, P. S.; Paape, N.; Kiefer, J.; Wasserscheid, P.; Leipertz, A. The role of the C2 position in interionic interactions of imidazolium based ionic liquids: a vibrational and NMR spectroscopic study. *Phys. Chem. Chem. Phys.* **2010**, *12* (42), 14153−14161.

(39) Batis, N. H.; Delichere, P.; Batis, H. Physicochemical and catalytic properties in methane combustion of $La_{1-x}Ca_xMnO_{3\pm y}$ ($0 \leq x \leq 1$; $-0.04 \leq y \leq 0.24$) perovskite-type oxide. *Appl. Catal., A* **2005**, *282* (1−2), 173−180.
(40) Liu, Y. S.; Li, J.; Li, W. Z.; Li, Y. M.; Chen, Q. Y.; Zhan, F. Q. Nitrogen-doped graphene aerogel-supported spinel $CoMn_2O_4$ nanoparticles as an efficient catalyst for oxygen reduction reaction. *J. Power Sources* **2015**, *299*, 492−500.
(41) Nesbitt, H. W.; Banerjee, D. Interpretation of XPS Mn(2p) spectra of Mn oxyhydroxides and constraints on the mechanism of MnO_2 precipitation. *Am. Mineral.* **1998**, *83* (3−4), 305−315.
(42) Banerjee, D.; Nesbitt, H. W. Oxidation of aqueous Cr(III) at birnessite surfaces: Constraints on reaction mechanism. *Geochim. Cosmochim. Acta* **1999**, *63* (11−12), 1671−1687.
(43) Biesinger, M. C.; Payne, B. P.; Grosvenor, A. P.; Lau, L. W. M.; Gerson, A. R.; Smart, R. S. C. Resolving surface chemical states in XPS analysis of first row transition metals, oxides and hydroxides: Cr, Mn, Fe, Co and Ni. *Appl. Surf. Sci.* **2011**, *257* (7), 2717−2730.
(44) Zhu, S.; Huo, W.; Liu, X.; Zhang, Y. Birnessite based nanostructures for supercapacitors: Challenges, strategies and prospects. *Nanoscale Adv.* **2020**, *2* (1), 37−54.
(45) Chien, S. W. C.; Chang, C. H.; Chen, S. H.; Wang, M. C.; Rao, M. M.; Veni, S. S. Oxidative degradation of pyrene in contaminated soils by δ-MnO_2 with or without sunlight irradiation. *Sci. Total Environ.* **2011**, *409* (19), 4078−4086.
(46) Zhang, Y.; Fu, J.; Cui, P.; Cheng, S.; Cui, X.; Qin, T.; Zhou, J.; Zhang, Z.; Su, Q.; Xie, E. Low-crystalline birnessite-MnO_2 nanograins for high-performance supercapacitors. *Electrochim. Acta* **2021**, *389*, 138761.
(47) Domínguez, A.; Malgaretti, P.; Popescu, M. N.; Dietrich, S. Effective interaction between active colloids and fluid interfaces induced by Marangoni flows. *Phys. Rev. Lett.* **2016**, *116* (7), 078301.
(48) Sun, X.; Luo, H.; Dai, S. Ionic liquids-based extraction: a promising strategy for the advanced nuclear fuel cycle. *Chem. Rev.* **2012**, *112* (4), 2100−2128.
(49) Cui, H.; Chen, J.; Li, H.; Zou, D.; Liu, Y.; Deng, Y. High-performance polymer-supported extractants with phosphonate ligands for scandium(III) separation. *AIChE J.* **2016**, *62* (7), 2479−2489.
(50) Zhang, H.; Li, A.; Li, K.; Wang, Z.; Xu, X.; Wang, Y.; Sheridan, M. V.; Hu, H.-S.; Xu, C.; Alekseev, E. V.; Zhang, Z.; Yan, P.; Cao, K.; Chai, Z.; Albrecht-Schonzart, T. E.; Wang, S. Ultrafiltration separation of Am(VI)-polyoxometalate from lanthanides. *Nature* **2023**, *616* (7957), 482−487.
(51) Wang, Z.; Dong, X.; Yan, Q.; Chen, J.; Xu, C. Separation of americium from curium through oxidation state control with record efficiency. *Anal. Chem.* **2022**, *94* (22), 7743−7746.
(52) Wang, Z.; Lu, J.-B.; Dong, X.; Yan, Q.; Feng, X.; Hu, H.-S.; Wang, S.; Chen, J.; Li, J.; Xu, C. Ultra-efficient americium/lanthanide separation through oxidation state control. *J. Am. Chem. Soc.* **2022**, *144* (14), 6383−6389.
(53) Dugoni, G. C.; Baggioli, A.; Famulari, A.; Sacchetti, A.; Martí-Rujas, J.; Mariani, M.; Macerata, E.; Mossini, E.; Mele, A. Structural properties of the chelating agent 2, 6-bis (1-(3-hydroxypropyl)-1, 2, 3-triazol-4-yl) pyridine: a combined XRD and DFT structural study. *RSC Adv.* **2020**, *10* (33), 19629−19635.
(54) De Vos, N.; Maton, C.; Stevens, C. V. Electrochemical stability of ionic liquids: General influences and degradation mechanisms. *Chemelectrochem* **2014**, *1* (8), 1258−1270.
(55) Zhou, H. M.; Shen, Y. Y.; Lv, P.; Wang, J. J.; Li, P. Degradation pathway and kinetics of 1-alkyl-3-methylimidazolium bromides oxidation in an ultrasonic nanoscale zero-valent iron/hydrogen peroxide system. *J. Hazard. Mater.* **2015**, *284*, 241−252.
(56) Lu, W. W.; Huang, Q. L.; Zhang, Y.; Yao, K. S.; Wang, J. J. Plasmon-enhanced photodegradation of ionic liquids with Ag nanocubes/ZnO microsphere composites. *Ind. Eng. Chem. Res.* **2018**, *57* (46), 15597−15605.
(57) Bocos, E.; González-Romero, E.; Pazos, M.; Sanroman, M. A. Application of electro-Fenton treatment for the elimination of 1-Butyl-3-methylimidazolium triflate from polluted water. *Chem. Eng. J.* **2017**, *318*, 19−28.
(58) Li, B. B.; Guo, R. X.; Tian, J.; Wang, Z. Y.; Qu, R. J. New findings of ferrate(VI) oxidation mechanism from its degradation of alkene imidazole ionic liquids. *Environ. Sci. Technol.* **2021**, *55* (17), 11733−11744.

https://doi.org/10.1021/acs.langmuir.4c00003
Langmuir 2024, 40, 6980−6989